



# CHORUS

This is the accepted manuscript made available via CHORUS. The article has been published as:

## Precise half-life measurement of the superallowed $\beta^{\{+\}}$ emitter $^{38}\text{Ca}$

H. I. Park, J. C. Hardy, V. E. Jacob, A. Banu, L. Chen, V. V. Golovko, J. Goodwin, V. Horvat, N. Nica, E. Simmons, L. Trache, and R. E. Tribble

Phys. Rev. C **84**, 065502 — Published 12 December 2011

DOI: [10.1103/PhysRevC.84.065502](https://doi.org/10.1103/PhysRevC.84.065502)

# Precise half-life measurement of the superallowed $\beta^+$ emitter $^{38}\text{Ca}$

H.I. Park,<sup>\*</sup> J.C. Hardy,<sup>†</sup> V.E. Iacob,<sup>‡</sup> A. Banu,<sup>§</sup> L. Chen, V.V. Golovko,<sup>¶</sup>  
J. Goodwin, V. Horvat, N. Nica,<sup>‡</sup> E. Simmons, L. Trache, and R.E. Tribble  
*Cyclotron Institute, Texas A&M University, College Station, Texas 77845-3366, USA*  
(Dated: November 15, 2011)

The half-life of  $^{38}\text{Ca}$ , a  $T_Z = -1$  superallowed  $0^+ \rightarrow 0^+ \beta^+$  emitter, has been measured to be 443.77(36) ms. In our experiment, pure sources of  $^{38}\text{Ca}$  were produced and the decay positrons detected in a high-efficiency  $4\pi$  proportional gas counter. Since the  $\beta^+$  decay of  $^{38}\text{Ca}$  feeds  $^{38}\text{K}^m$ , which is itself a superallowed  $\beta^+$  emitter, the data were analyzed as a linked parent-daughter decay. Our result, with a precision of 0.08%, is a factor of five improvement on the best previous result.

PACS numbers: 21.10.Tg, 23.40.-s, 27.30.+t

## I. INTRODUCTION

At present, measurements of superallowed  $0^+ \rightarrow 0^+$  nuclear Fermi  $\beta^+$  decay lead to the most precise value for  $V_{ud}$ , the up-down quark-mixing element of the Cabibbo-Kobayashi-Maskawa (CKM) matrix. The unitarity of this matrix is a fundamental requirement of the electroweak Standard Model and currently the sum of squares of the experimentally determined top-row elements of the CKM matrix satisfies the unitarity condition within an uncertainty of  $\pm 0.06\%$  [1], which correspondingly limits the scope of possible new physics. Since  $V_{ud}$  is the dominant contributor to this sum, its precision is of crucial importance to the unitarity test, and its impact on searches for new physics motivates continued improvements to the experimental input data. To date, the  $ft$  values for ten different superallowed transitions have been measured to  $\sim 0.1\%$  precision and three more are known to  $\leq 0.3\%$  [2]. The work reported here is part of our program to increase the number of precisely measured transitions, particularly focusing on the decays of  $T_Z = -1$  nuclei.

The  $ft$  value for a  $T=1$  superallowed  $0^+ \rightarrow 0^+$  transition is directly related to the vector coupling constant  $G_V$  via the relation [2]:

$$\mathcal{F}t \equiv ft(1 + \delta'_R)(1 + \delta_{NS} - \delta_C) = \frac{K}{2G_V^2(1 + \Delta_R^V)}, \quad (1)$$

where  $\mathcal{F}t$  is defined to be the “corrected”  $ft$  value and  $K/(\hbar c)^6 = 2\pi^3 \hbar \ln 2 / (m_e c^2)^5 = 8120.2787(11) \times 10^{-10} \text{ GeV}^{-4} \text{ s}$ . Four small theoretical correction terms are included in the equation to take account of isospin-symmetry breaking and unobserved radiative effects:  $\delta_C$  is the correction for isospin-symmetry breaking;

$\Delta_R^V$  is the transition-independent part of the radiative correction; and  $\delta'_R$  and  $\delta_{NS}$  are the transition-dependent parts of the radiative correction, the former being a function only of the maximum positron energy and the atomic number,  $Z$ , of the daughter nucleus, while the latter, like  $\delta_C$ , depends in its evaluation on the details of nuclear structure. Although these calculated corrections are only of order  $\sim 1\%$  [3], they are significant when compared to the present level of experimental precision. Consequently, it is important to establish the reliability of the calculations.

Fortunately there is a powerful method for testing the reliability of the nuclear-structure-dependent correction terms,  $\delta_C$  and  $\delta_{NS}$ : Do they lead to consistent  $\mathcal{F}t$  values for all measured transitions? The uncorrected  $ft$  values for the 13 most precisely measured transitions scatter over a range of nearly 2%, yet the corrected  $\mathcal{F}t$  values must be statistically consistent with one another if the conserved vector current (CVC) hypothesis is to be satisfied. The requirement that CVC must be satisfied has been shown to be a sensitive test of the validity of the calculated structure-dependent correction terms, a test that so far has only been successfully passed by the set of calculations that is based on the effective-interaction shell model combined with Saxon-Woods radial wave functions (SM-SW) [4].

The case of  $^{38}\text{Ca}$ —a nucleus whose superallowed decay is not yet fully characterized—is particularly interesting as an extension of this test, since its total nuclear-structure-dependent correction is calculated with the SM-SW model to be  $\delta_C - \delta_{NS} = 0.94(7)\%$ , one of the largest in the  $sd$  shell [3]. If, with such a large correction, the measured  $ft$  value for  $^{38}\text{Ca}$  were also to yield a corrected  $\mathcal{F}t$  value consistent with the average established from the 13 currently best-known cases, then it would become a further powerful experimental validation of the calculated corrections. Essential to this test and to placing  $^{38}\text{Ca}$  on the same footing as the other well-known cases is a measurement of the  $ft$  value for its superallowed  $0^+ \rightarrow 0^+$  beta transition with  $\sim 0.1\%$  precision or better.

The  $ft$  value that characterizes the strength of any  $\beta$  transition depends on three measured quantities: the total transition energy,  $Q_{EC}$ ; the half-life,  $t_{1/2}$ , of the

<sup>\*</sup> hpark@comp.tamu.edu

<sup>†</sup> hardy@comp.tamu.edu

<sup>‡</sup> On leave from the National Institute for Physics and Nuclear Engineering “Horia Hulubei”, Bucharest, Romania.

<sup>§</sup> Current address: Department of Physics and Astronomy, James Madison University, Harrisonburg, VA 22807

<sup>¶</sup> Present address: Department of Physics, Queen’s University, Stirling Hall, Kingston, ON, K7L 3N6, Canada.

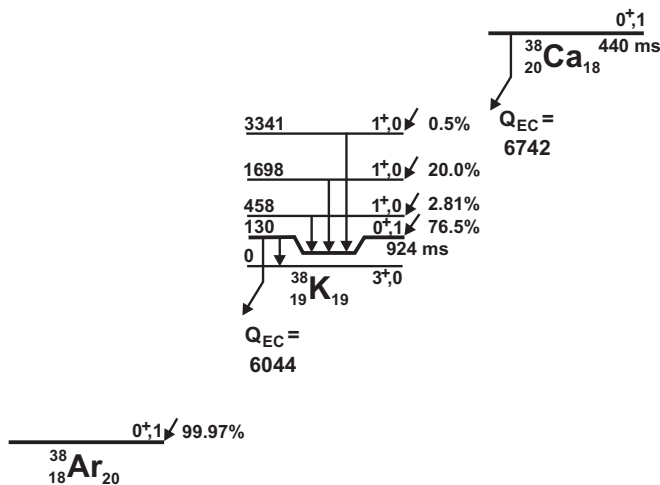


FIG. 1. Decay schemes of  $^{38}\text{Ca}$  and  $^{38}\text{K}^m$  showing only those features relevant to their superallowed  $\beta$  decays. All energies are in keV, and the  $Q_{EC}$  values shown are for the superallowed branches. The data are adopted from Ref. [9], in which the measured relative  $\beta$ -branching ratios for  $^{38}\text{Ca}$  were normalized to a calculated value for the superallowed branch. Three weak  $\beta$  branches from  $^{38}\text{Ca}$  to higher excited states have been omitted: their branching ratios total  $<0.2\%$ . Note that there is a  $0.03\%$   $\gamma$ -decay branch from the isomeric state  $^{38}\text{K}^m$  to the  $^{38}\text{K}$  ground state [10].

parent state; and the branching ratio,  $R$ , for the particular transition of interest. The value of  $Q_{EC}$  is used to determine the statistical rate function,  $f$ , while  $t_{1/2}$  and  $R$  are combined to obtain the partial half-life,  $t$ . Before our half-life measurement of  $^{38}\text{Ca}$ , which is reported here, only its  $Q_{EC}$  value was known to the desired precision: it had been measured with Penning-traps to  $\pm 0.006\%$  [5–7], which corresponds to an  $f$ -value precision of  $\pm 0.03\%$  [2]. The most precise half-life result was only known to  $\pm 0.4\%$  [8] and the superallowed branching ratio has not yet been measured at all.

As seen in Fig. 1, the decay of  $^{38}\text{Ca}$  feeds  $^{38}\text{K}^m$ , which is also a superallowed emitter with a half-life that is 2.1 times longer than that of  $^{38}\text{Ca}$ . To achieve high precision under these circumstances we need to produce high-purity  $^{38}\text{Ca}$  samples, with no initial contribution from  $^{38}\text{K}^m$ ; and we must use the specialized analysis techniques that we developed previously for our studies of other linked parent-daughter decays, those of  $^{34}\text{Ar}$  [11] and  $^{26}\text{Si}$  [12]. Our approach will be described briefly in the following sections, but for further detail the reader is referred to those two earlier publications.

## II. EXPERIMENT

### A. Production of $^{38}\text{Ca}$

We obtained  $^{38}\text{Ca}$  via the inverse-kinematics reaction,  $p(^{39}\text{K}, 2n)^{38}\text{Ca}$ . A  $^{39}\text{K}$  beam, produced with 30 MeV

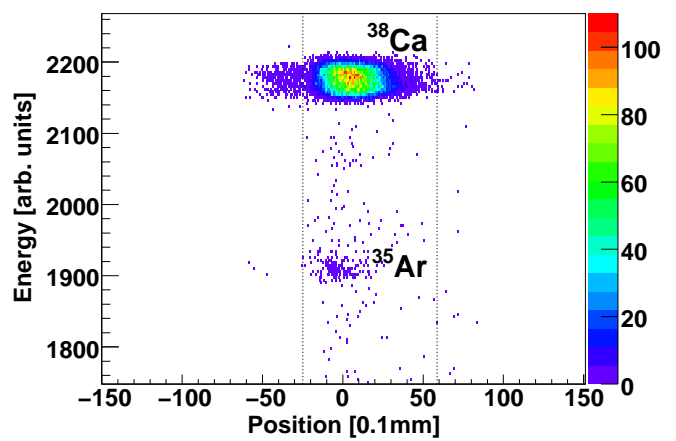


FIG. 2. (Color online) Deposited energy versus position as recorded in the PSSD at the MARS focal plane. This result was obtained after the spectrometer had been tuned for  $^{38}\text{Ca}$ . The dashed lines show the position of the extraction slits, 8.4 mm apart, which we used during these measurements. Note that the tail to the left of the main  $^{38}\text{Ca}$  peak is an artifact caused by incomplete charge collection in strip detector. From such spectra recorded periodically during our experiment, we determined that the extracted  $^{38}\text{Ca}$  beam included a  $0.6\%$  contribution from  $^{35}\text{Ar}$ .

per nucleon by the K500 superconducting cyclotron at Texas A&M University, bombarded a 2-atm hydrogen gas target cooled to liquid nitrogen temperature. The fully stripped  $^{38}\text{Ca}$  ejectiles were separated by their charge-to-mass ratio,  $q/m$ , with the Momentum Achromat Recoil Spectrometer (MARS) [13]. Initially working with a low-current primary beam, we inserted a 1-mm-thick 16-strip position-sensitive silicon detector (PSSD) at the focal plane of MARS. This detector was used first for the identification of secondary reaction products, then for the control of the selection and focus of  $^{38}\text{Ca}$  in the center of the beam line. Fig. 2 shows the energy deposited in the detector versus position in the focal plane. This gives a clear indication of any nearby reaction products that could potentially contribute as impurities to our extracted beam. In this case, only  $^{38}\text{Ca}$  and a very weak contribution from  $^{35}\text{Ar}$  appear;  $^{38}\text{K}^m$  is far off scale to the left and can be completely excluded. With the focal-plane acceptance slits set to a width of 8.4 mm (dashed lines in Fig. 2), the  $^{35}\text{Ar}$  contribution to the total extracted beam was determined to be  $0.6\%$ .

After the tune-up procedures had been completed, we removed the PSSD and increased the primary beam intensity. The  $^{38}\text{Ca}$  beam from the acceptance slits then exited the vacuum system through a  $51\text{-}\mu\text{m}$ -thick Kapton window, passed through a  $0.3\text{-mm}$ -thick BC404 scintillator, used to count the ions, and then through a stack of aluminum degraders, finally stopping in the  $76\text{-}\mu\text{m}$ -thick aluminized Mylar tape of a fast tape-transport system. The combination of  $q/m$  selectivity in MARS and range separation in the degraders provided implanted samples that we determined to be better than  $99.6\%$  pure.

After we had collected  $^{38}\text{Ca}$  for 1 s, the cyclotron beam was interrupted and the collected sample moved in 198 ms to the center of a  $4\pi$  proportional gas counter located in a well-shielded area about 90 cm away. The decay positrons detected from the gas counter were multiscaled for 15 s into two separate 500-channel time spectra, each corresponding to a different pre-set dominant dead-time. Note that the 15-s count period is equivalent to 34 half-lives of  $^{38}\text{Ca}$  or 16 half-lives of its daughter  $^{38}\text{K}^m$ . These collect/move/count cycles were controlled by the tape-transport system, and their timing was continuously monitored on-line by the data-acquisition computer. The cycles were repeated until the desired overall statistics had been achieved.

### B. Gas counter and electronics

The  $4\pi$  proportional gas counter is the same one we have used in previous precise half-life measurements (*e.g.* Refs. [11, 12]). It consists of two separate gas cells machined from copper, which, when assembled, have a 0.25-mm slot between them, through which the Mylar transport-tape passes. Each cell contains a 13- $\mu\text{m}$ -diameter gold-plated tungsten wire along the central axis, which was connected through insulators to positive high voltage. On the side facing the tape, each cell has a 3.7-cm-diameter entrance window sealed with 1.5- $\mu\text{m}$ -thick Havar foil. Methane at  $\sim 1$  atm flowed continuously through each gas cell. Methane offers adequate gas gain for detecting positrons and is quite insensitive to  $\gamma$  rays.

Signals from the gas counter were fed into a preamplifier and fast timing-filter amplifier set to high gain ( $\times 500$ ). After the first stage of amplification in the amplifier, we have inserted a Schottky diode to clip large pulses that would otherwise have saturated the amplifier and delayed its recovery. The clipped and amplified signals were then input to a discriminator with very low threshold (150-250 mV). The discriminator output was then split and passed to two fixed-width, nonextending gate generators, which imposed different dominant dead times in two parallel multiscaled data streams. The time increment per channel for the multichannel scalars was externally controlled by a function generator accurate to 0.01 ppm. We continuously monitored the two different dead times (gate widths) to an accuracy of  $\pm 5$  ns by scaling signals from a constant-frequency pulse generator recorded in coincidence with the gating signals in each data stream. Having these two data streams allowed us to test that our dead-time corrected results were independent of the actual dead time of the circuit. A more detailed description of our electronic arrangement can be found in Ref. [11].

Before our measurement, the safe operating range for the detector bias voltage was determined with a  $^{90}\text{Sr}/^{90}\text{Y}$   $\beta$  source, which had been prepared on a sample length of transport tape. Positioning this  $\beta$  source in the slot between the two halves of the detector—exactly where

the  $^{38}\text{Ca}$  sample is delivered on-line—we measured the counting rate as a function of the applied detector voltage at the three different thresholds used in our half-life measurements (150, 200 and 250 mV). Initially, as the applied voltage is raised the count-rate also rises since the increasing gas gain leads to more primary ionizing  $\beta$  events triggering the discriminator. However, at approximately 2600 volts—the exact value depends on the threshold setting—a “plateau” is reached, and the count rate remains nearly unchanged for the next 200-300 volts increase in the bias voltage. At higher voltages still, there is a second rapid rise in the count rate as spurious pulses increasingly trigger the discriminator. During our  $^{38}\text{Ca}$  measurement the detector was always operated in the plateau region as determined in advance with the  $^{90}\text{Sr}/^{90}\text{Y}$  source. Under these conditions, the detector efficiency was close to 100% and was essentially independent of count rate. Also, the background rate at our shielded counting location was  $\sim 1$  count/s, which is 3-4 orders of magnitude lower than the initial count rate for each collected sample.

### C. Special precautions

As the experiment was aimed at 0.1% precision, many tests for systematic effects were made and special precautions taken during the measurements themselves:

- (i) Every experiment was subdivided into many separate runs, differing only in their particular combination of detection parameters: dominant dead-time, detector bias, and discrimination threshold. We used combinations of four different dead times (3, 4, 6, and 8  $\mu\text{s}$ ), three discriminator thresholds (150, 200, and 250 mV) and three detector biases (2600, 2700, and 2800 V). The separate analysis of each individual run allowed us to test for systematic effects that could contribute to the uncertainty in the final result.
- (ii) Since each  $^{38}\text{Ca}$  decay produces a  $^{38}\text{K}^m$  daughter that also decays, the ratio of the parent to daughter activities depends on the time-dependence of the rate at which  $^{38}\text{Ca}$  accumulates in the tape during the collection period. The number of ions registered in the scintillator located just in front of the aluminum degraders (see Sec. II A) was recorded as a function of time with each cycle, and the results were used in our analysis.
- (iii) The tape-transport system is quite consistent in placing the collected source within  $\pm 3$  mm of the center of the detector, but it is a mechanical device, and occasionally larger deviations occur. We separately recorded the number of nuclei detected in the scintillator during the collection period of each cycle, and the number of positrons detected in the gas counter during the subsequent count period. The

ratio of the latter to the former is a sensitive measure of whether the source was seriously misplaced in the proportional counter.

- (iv) We checked the composition of the beam exiting MARS on a daily basis by reinserting the PSSD at the MARS focal plane. No appreciable changes were observed.
- (v) A background measurement was made in which all conditions were identical to those of a normal run except that the tape motion was disabled.
- (vi) In one run, we collected activity for 4 s and counted for 40 s in repeated cycles in order to search for long-lived impurities. Apart from  $^{38}\text{Ca}$ , only the decay of  $^{35}\text{Ar}$  ( $t_{1/2} = 1775.4$  ms) was evident (see Sec. III C).

### III. ANALYSIS AND RESULTS

For this measurement, over 125 million  $\beta$  events were obtained from 11,271 cycles divided into 32 separate runs. Before analyzing the data, we first removed any cycles that had fewer than 500  $\beta$ -particles detected by the gas counter, which indicated little—or no—primary beam from the cyclotron during the collection period. We then excluded cycles that had an anomalously low ratio of recorded  $\beta$ -particles to implanted  $^{38}\text{Ca}$  ions as observed in the scintillator. A low ratio is indicative of faulty tape motion leading to a misplaced sample in the gas detector. As a result of these pre-selections, approximately 11% of the cycles were rejected from all 32 runs, 7% for low or no beam and 4% for a misplaced sample. The remaining data were corrected cycle-by-cycle for dead-time losses based on the method described in Ref. [14]. The final decay spectrum for each run was then obtained from the sum of the dead-time corrected decay spectra from all accepted cycles in that run.

The total time-decay spectrum obtained from the combined runs is presented in Fig. 3, where we also show the separate contributions from the  $^{38}\text{Ca}$  parent and  $^{38}\text{K}^m$  daughter. This breakdown into components is based upon our final analysis and is presented here simply to illustrate how the parent-daughter decay curve, which combines two rather similar half-lives, tends to mask the parent half-life even though the parent activity dominates at the start of the counting period.

#### A. Parent-daughter connection

The total positron activity from the combined decays of  $^{38}\text{Ca}$  and its daughter  $^{38}\text{K}^m$  can be described by the coupled decay equations:

$$\Lambda_{total} = C_1 e^{-\lambda_1 t} + C_2 e^{-\lambda_2 t}, \quad (2)$$

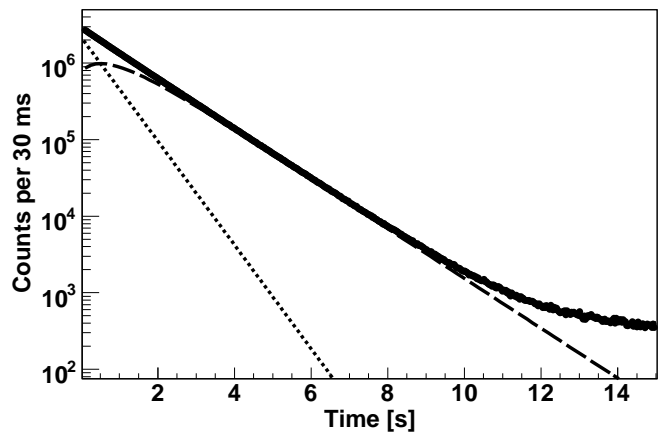


FIG. 3. Measured time-decay spectrum (solid line) for the total of all data obtained from the  $\beta^+$  decay of  $^{38}\text{Ca}$  and its daughter  $^{38}\text{K}^m$ . The dotted/dashed lines represent the derived  $^{38}\text{Ca}/^{38}\text{K}^m$  contributions.

with

$$\begin{aligned} C_1 &= N_1 \epsilon_2 \lambda_1 \left( \frac{\epsilon_1}{\epsilon_2} - \frac{\lambda_2}{\lambda_1 - \lambda_2} \right) \\ C_2 &= N_1 \epsilon_2 \lambda_2 \left( \frac{N_2}{N_1} + \frac{\lambda_1}{\lambda_1 - \lambda_2} \right) \end{aligned} \quad (3)$$

where  $t$  is the time elapsed after the end of the collection period;  $N_{1,2}$  are the numbers of  $^{38}\text{Ca}$  and  $^{38}\text{K}^m$  nuclei present in the sample at  $t = 0$ ;  $\epsilon_{1,2}$  are the experimental efficiencies for detecting the positrons from the respective decays; and  $\lambda_{1,2}$  are the corresponding decay constants.

When  $\lambda_1 = 2\lambda_2$  (and  $\epsilon_1 = \epsilon_2$ ) the coefficient  $C_1$  vanishes, leaving a single exponential term having the decay constant of the daughter. This is very nearly the case for the decays of  $^{38}\text{Ca}$  and  $^{38}\text{K}^m$ , which have decay constants that are related by a factor of 2.1. Consequently, for our measurements, the coefficient  $C_1$  is more than a factor of 10 smaller than  $C_2$ . The impact is clearly evident in Fig. 3 where the growth and decay of the daughter activity almost completely masks the decay of the parent. This imposes a serious limitation on the precision that can be obtained from a free fit to the data. Even with  $\lambda_2$  fixed at its known value,  $C_1$ ,  $C_2$ , and  $\lambda_1$  (as well as the constant background) must all be determined independently, which leads to a  $\lambda_1$  with very large uncertainty.

This deficiency can be overcome by application of the technique we developed based on the maximum-likelihood method and used in our previous measurements of the half-lives of  $^{34}\text{Ar}$  [11] and  $^{26}\text{Si}$  [12], which have similar coupled decays. The key element is to fix the ratio of  $C_2/C_1$  so that the number of adjustable parameters in the fit is reduced to three (including background). To achieve this we must determine the two ratios,  $N_2/N_1$  and  $\epsilon_1/\epsilon_2$ , from our experimental parameters.

If the  $^{38}\text{Ca}$ -sample collection rate were exactly constant, it would be a simple matter to calculate the  $N_2/N_1$  ratio from the production of  $^{38}\text{K}^m$  (via  $^{38}\text{Ca}$  decay) over

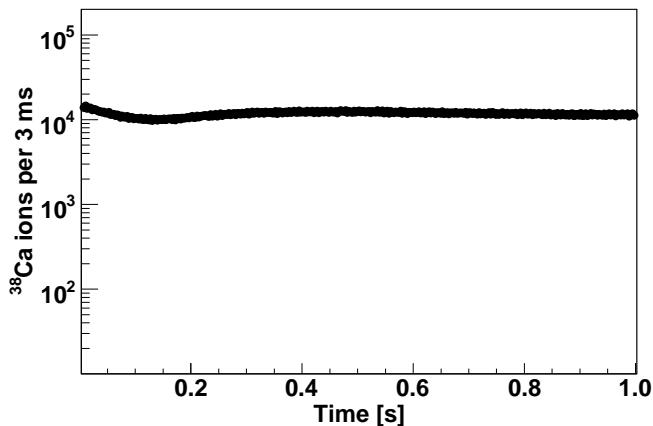


FIG. 4. Typical time-profile of the collected  $^{38}\text{Ca}$  beam measured over the course of one run. The initial drop in intensity is generated by the decrease in local density of the hydrogen in the target cell as the primary beam heats the gas around its path. A fan located inside the gas-target mitigates the effect and ensures a rapid transition to stable conditions.

the collection period. Instead of relying on approximate constancy, though, we recorded as a function of time the number of  $^{38}\text{Ca}$  ions detected by the scintillator at the exit of MARS for each individual cycle. As shown in Fig. 4, there is an appreciable variation in the collection rate over the first third of each collection period, caused by local heating and a concomitant drop in gas density along the path of the primary beam. Although the fan-assisted recovery to steady-state conditions is relatively fast, the initial variation is enough to make a change in the ratio  $N_2/N_1$ . We also found that the size of the variation depended on the primary beam intensity, thus potentially changing the beam time-profile from one cycle to another. However, with the collection-rate profile recorded, we could accurately calculate the  $N_2/N_1$  ratio for each run by obtaining the decay-production of  $^{38}\text{K}^m$  from a numerical integration that incorporated the measured  $^{38}\text{Ca}$  collection rate. This calculation of course depends on  $\lambda_1$  (also on  $\lambda_2$ ) so, in practice, when we fitted our decay data, this calculation was incorporated into the fitting function, with  $\lambda_1$  being common to the ratio determination and the calculated decay curve.

### B. Parent-daughter relative efficiencies

For the coupled decays of  $^{38}\text{Ca}$  and  $^{38}\text{K}^m$ , it might easily be assumed that the efficiency ratio,  $\epsilon_1/\epsilon_2$ , equals unity since both activities were observed with identical geometry, a very low electronic threshold and nearly 100% overall efficiency. As described in Sec. II B, we operate our gas counter at  $\times 500$  gain and with clipped pulses so, at  $\leq 250$  mV, the electronic threshold is low enough to be considered negligible. However, there is also a threshold energy arising from the fact that low-energy positrons are stopped in the aluminized Mylar

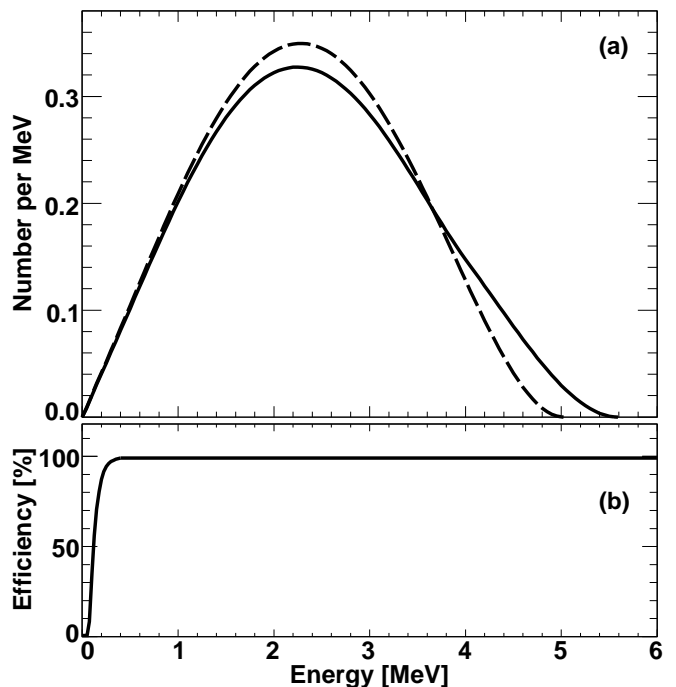


FIG. 5. (a) Calculated  $\beta^+$  energy spectra for  $^{38}\text{Ca}$  (solid curve) and  $^{38}\text{K}^m$  (dashed curve), each normalized to unity. The former includes the Gamow-Teller branches to  $1^+$  states as well as the superallowed branch to the  $0^+$  isomer; the latter is a pure superallowed decay (see Fig.1 for both decay schemes). (b) System efficiency for detecting positrons due to the effects of the aluminized Mylar tape and the Havar windows of the detector gas cells. The curve is the result of a Monte Carlo calculation with the EGSnrc code.

transport-tape (half-thickness,  $38\ \mu\text{m}$ ) and in the Havar windows of the gas counter ( $1.5\ \mu\text{m}$  thick), never reaching the active volume of the detector. The impact of this effective threshold on the efficiency ratio becomes significant when the end-points and/or shapes of the parent and daughter  $\beta$  spectra are significantly different from one another [12].

Fig. 5(a) presents calculated  $\beta$  spectra for  $^{38}\text{Ca}$  and  $^{38}\text{K}^m$ , with end-point energies of 5590 keV and 5022 keV respectively. The Gamow-Teller branches are included along with the superallowed branch for the  $^{38}\text{Ca}$  spectrum; only the superallowed branch contributes to the decay of  $^{38}\text{K}^m$ . In principle, for two such decays with different end-points, a low-energy cutoff removes a different fraction from each decay, leading to different effective efficiencies for detecting them. In practice, for the  $^{38}\text{Ca}$  and  $^{38}\text{K}^m$  decays, the lower energy Gamow Teller branches contributing to the former alter its spectrum shape enough that a small low-energy cutoff has nearly the same effect on both decays.

To evaluate the exact effect of the cutoff we modeled our exact tape/window/detector geometry within the Monte Carlo code EGSnrc (version V4-r2-3-0) [15] and calculated the overall system efficiency as a function

of positron energy. The result is shown in Fig. 5(b). Because the decay positrons are emitted isotropically, their paths through the tape and window cover a range of lengths, resulting in a low-energy cut-off that is not sharp, as is evident in the figure. We convoluted the Monte Carlo result with each of the two  $\beta^+$  spectra in Fig. 5(a) to obtain our overall efficiencies for detecting the parent and the daughter activities. The deduced efficiency ratio was  $\epsilon_1/\epsilon_2 = 1.00042(5)$ , where we have also incorporated the fact that  $^{38}\text{K}^m$  has a 0.033(4)%  $\gamma$ -decay branch that competes with the superallowed decay branch [10]. The uncertainty we quote on our efficiency ratio arises mostly from the uncertainty on the  $^{38}\text{K}^m$   $\gamma$ -decay branch but also from our assigning a  $\pm 10\%$  relative uncertainty on the calculated ranges. This result for the efficiency ratio was used in the analysis of all runs.

### C. Sample impurity

Based on the spectrum of reaction products identified at the MARS focal plane (see Fig. 2), we determined that  $^{35}\text{Ar}$  ( $t_{1/2} = 1775.4$  ms) was present in our extracted beam with an intensity of 0.6% relative to that of  $^{38}\text{Ca}$ . However, the amount of  $^{35}\text{Ar}$  actually collected in the Mylar transport tape could be reduced further because  $^{35}\text{Ar}$  loses slightly less energy than  $^{38}\text{Ca}$  in traversing the aluminum degraders. With careful adjustment, we could retain virtually all the  $^{38}\text{Ca}$  nuclei in the transport tape while letting at least some of the  $^{35}\text{Ar}$  nuclei pass all the way through the tape. Note that the ranges of the  $^{35}\text{Ar}$  and  $^{38}\text{Ca}$  nuclei are unaffected by temporal changes in the target-gas density (see Fig. 4) since one of the series components of the MARS spectrometer is a velocity filter. Furthermore, the energy loss of the primary beam in the 10-cm-long gas target is  $\sim 2.5$  MeV per nucleon, and the observed temporal density changes would briefly alter the average energy of the beam in the gas by less than 150 keV per nucleon. This would have no appreciable effect on the relative production cross sections of  $^{35}\text{Ar}$  and  $^{38}\text{Ca}$ .

To optimize conditions, at the beginning of the experiment we measured the amount of  $^{38}\text{Ca}$  activity collected in the tape as a function of degrader thickness. This allowed us to determine the depth distribution of  $^{38}\text{Ca}$  in the tape and to verify that its spread in depth corresponded to the momentum spread as set by the momentum slits in MARS. Based on our measurement we could also determine the thickness of aluminum degraders required to place the collected  $^{38}\text{Ca}$  activity exactly mid-way through the tape. The experimentally determined degrader thickness to achieve this was very close to the thickness we had calculated with the SRIM code [16]. This result verified the reliability of the code and gave us confidence to use it to determine the depth distribution of  $^{35}\text{Ar}$  relative to that of  $^{38}\text{Ca}$ . Unfortunately the code indicated that, with the stopped  $^{38}\text{Ca}$  nuclei located mid-way through the Mylar tape, the  $^{35}\text{Ar}$  would still be

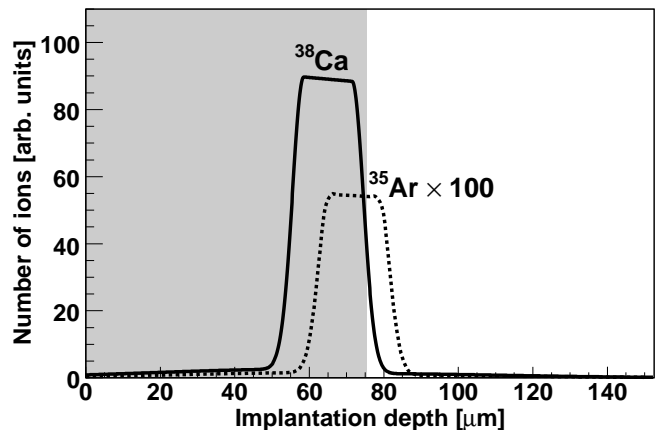


FIG. 6. The calculated implantation profiles of  $^{38}\text{Ca}$  (solid line) and  $^{35}\text{Ar}$  (dashed line) in and beyond the Mylar tape, under the conditions applying to our half-life measurements. The beams enter from the left. The shaded region corresponds to the actual thickness of our collection tape: all ions within the shaded region are collected in our sample; all others are not.

entirely in the tape as well, albeit nearer the back of it.

Accordingly, for our half-life measurements we reduced the thickness of aluminum degraders so as to deposit the  $^{38}\text{Ca}$  at the back of the tape. A representation of the situation is given in Fig. 6. The depth distribution shown for  $^{38}\text{Ca}$  was derived from our measurement of activity versus degrader thickness, and the implantation depth of  $^{35}\text{Ar}$  relative to  $^{38}\text{Ca}$  was the result of the SRIM calculation. Even with the  $^{38}\text{Ca}$  nuclei implanted as deep as possible in the tape, the figure shows that approximately 75% of the  $^{35}\text{Ar}$  nuclei in the beam extracted from MARS remained in the collection tape. Based on the relative intensities measured in the MARS focal plane (see Sec. II A), this corresponds to an  $^{35}\text{Ar}/^{38}\text{Ca}$  ratio of 0.45% in the collected samples. Unfortunately this cannot be considered a very precise result: an increase of only  $3\ \mu\text{m}$  in the depth of the implanted ions relative to the edge of the tape in Fig. 6 would change the ratio to 0.35%. We therefore sought a more precise method to determine the  $^{35}\text{Ar}$  contribution.

To this end, we turned to the decay spectrum obtained with longer collect and count times (see item (vi) in Sec. II C). Because the half-life of  $^{35}\text{Ar}$  is four times that of  $^{38}\text{Ca}$ , a longer collect time ensured that the contribution of  $^{35}\text{Ar}$  to our collected samples would be enhanced, and a longer count time made us more sensitive to its decay. As expected, in addition to  $^{38}\text{Ca}$ , the decay of  $^{35}\text{Ar}$  was clearly identifiable in the measured decay spectrum. No other impurities were found. We then fit the spectrum with four components:  $^{38}\text{Ca}$ ,  $^{38}\text{K}^m$ ,  $^{35}\text{Ar}$ , and a constant background. The half-lives of  $^{35}\text{Ar}$  and  $^{38}\text{K}^m$  were fixed at 1775.4 ms [11] and 924.33 ms [2] respectively. The half-life of  $^{38}\text{Ca}$  was also fixed for each fit, but we performed a number of fits with its half-life fixed to different values between 442 and 445 ms. This range was greater than the

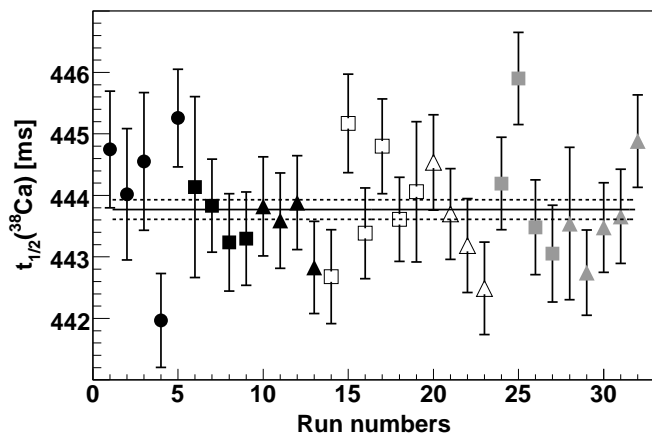


FIG. 7. Test for possible systematic bias in the  $^{38}\text{Ca}$  half-life measurement due to discriminator threshold or detector voltage. Black/open/grey symbols represent the three discriminator settings, 150 mV/200 mV/250 mV; the three detector biases, 2600 V, 2700 V and 2800 V are represented by the symbol shapes  $\circ$ ,  $\square$  and  $\triangle$ , respectively. The average value for the half-life is 443.77(16) ms (statistical uncertainty only) with  $\chi^2/ndf = 40/31$ . The average value appears as the solid line, with dashed lines as uncertainty limits.

range of half-life values we obtained from an analysis of the short collect-and-count-time data (see following section), in which we considered  $^{35}\text{Ar}$  impurity levels from 0.2% to 0.6%, the maximum possible. The impurity level obtained from the fits to the long collect-and-count-time data turned out to be very insensitive to the half-life assumed for  $^{38}\text{Ca}$ , allowing us to determine the  $^{35}\text{Ar}/^{38}\text{Ca}$  ratio to be 0.36(5)% at the beginning of the collection period. This is the value we subsequently used for our final analysis of the short collect-and-count-time data.

#### D. Time decay analysis

Data from 32 separate runs were fitted with the linked parent-daughter decay equations presented in Sec. III A, to which were added terms incorporating the  $^{35}\text{Ar}$  impurity and a constant background. The half-life of  $^{38}\text{K}^m$  was fixed at its known value of 924.33 ms [2] and the ratio of its initial activity to that of  $^{38}\text{Ca}$  was obtained for each run from numerical integration of the measured  $^{38}\text{Ca}$  beam profile as a function of time in that run (see Sec. III A and Fig. 4). The efficiency ratio  $\epsilon_1/\epsilon_2$  was fixed at 1.00042, the value established in Sec. III B. Finally, the  $^{35}\text{Ar}$  half-life was also set to its known value of 1775.4 ms [11] and its initial relative activity was set to 0.36%, the value determined in Sec. III C.

Since we operate our proportional gas counter safely in the proportional region, we have no reason to expect our results to depend on detection parameters. However, because each run was obtained under a different combination of detecting conditions, we could actually test for such systematic effects by comparing the individually

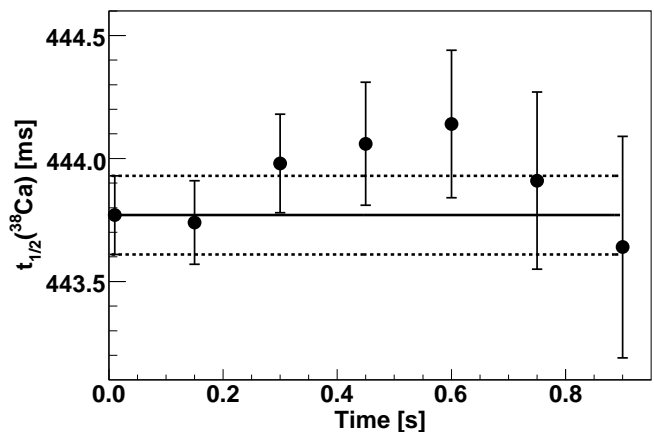


FIG. 8. Test for possible systematic bias in the  $^{38}\text{Ca}$  half-life measurement caused by short-lived impurities or by rate-dependent counting losses that we have not accounted for. Each point is the result of a separate fit to the data; the abscissa for each point represents the time period at the beginning of the counting cycle for which the data were omitted from that particular fit. The solid and dashed lines correspond to the average half-life value and uncertainties given in Fig. 7.

fitted half-lives of  $^{38}\text{Ca}$  obtained from each run. As displayed in Fig. 7 the half-life results confirm that there was no dependence on either the applied bias voltages or the discriminator threshold settings. Although not illustrated, the results were also independent of the four different dominant dead times that were imposed in different runs. A further test, sensitive to the possible presence of undetected short-lived impurities or counting-rate dependent effects, is illustrated in Fig. 8. We removed data from the first 150 ms of the counting period and refitted the remaining data; then we removed an additional 150 ms of data and refitted again. We continued this procedure until 900 ms of data had been removed. The figure demonstrates that the half-lives extracted under these conditions were consistent with one another within statistical uncertainties.

With these possible systematic effects eliminated as significant factors, our result for the  $^{38}\text{Ca}$  half-life is determined to be  $t_{1/2}(^{38}\text{Ca}) = 443.77$  ms, with a statistical uncertainty of  $\pm 0.16$  ms. The normalized  $\chi^2$  of this average is 1.29, and the statistical uncertainty just quoted already includes multiplication by the square root of the normalized  $\chi^2$ .

#### E. Uncertainty budget

Naturally, other factors beyond counting statistics contribute to the overall uncertainty. We itemize the ones we are aware of in Table I. The largest contribution comes from the uncertainty in the intensity of the  $^{35}\text{Ar}$  impurity in the sample (see Sec. III C). The second largest is due to the uncertainty in the  $^{38}\text{K}^m$  half-life. Because we

TABLE I. Error budget for the  $^{38}\text{Ca}$  half-life measurement.

Source	Uncertainty (ms)
statistics	0.16
sample impurity ( $^{35}\text{Ar}$ )	0.23
$t_{1/2}(^{38}\text{K}^m)$	0.22
efficiency ratio, $\epsilon_1/\epsilon_2$	0.01
Total	0.36
<hr/>	
$^{38}\text{Ca}$ half-life result (ms)	443.77(36)

are dealing with a coupled parent-daughter decay, the fitted half-life obtained for the parent ( $^{38}\text{Ca}$ ) depends strongly on the half-life used for the daughter ( $^{38}\text{K}^m$ ) in the fitting process. The value we used, 924.33(27) ms, was taken from the most recent review of superallowed  $\beta$  decays [2] and is the average of the six previous measurements quoted with better than  $\sim 0.1\%$  precision. The final contribution to our error budget is the one associated with the different efficiencies for detecting parent and daughter activities; it is very small because the ratio itself is so close to unity that it plays only a very minor role for this particular pair of decays. Our final result for the half-life of  $^{38}\text{Ca}$  is 443.77(36) ms.

#### F. Comparison with previous results

Four out of the five previous measurements of the  $^{38}\text{Ca}$  half-life were made before 1980 and with quoted uncertainties more than thirty times larger than ours: 470(20) ms [17], 439(12) ms [18], 450(70) ms [19] and 430(12) ms [20]. These were each obtained by observation and analysis of the decay of  $\beta$ -delayed  $\gamma$ -rays from the daughter,  $^{38}\text{K}$ . The first result lies about one-and-a-half of its error bar away from our quoted half-life; the other three agree well within their error bars. There is a much more recent measured value, 443.8(19) ms [8], which was obtained in a similar manner to ours, from a measurement of the decay positrons in a gas counter; in their case, though, sample purity was achieved by collecting the  $^{38}\text{Ca}$  first in a Penning trap. Our half-life result agrees well with theirs but with an uncertainty five times smaller.

## IV. CONCLUSIONS

We report here the half-life of the superallowed  $\beta^+$  emitter  $^{38}\text{Ca}$  to be 443.77(36) ms, the first time it has been measured with a precision of better than 0.1%. Since  $^{38}\text{Ca}$  and its daughter  $^{38}\text{K}^m$  are both positron emitters and have comparable half-lives, we analyzed their decay using a technique we developed previously [11, 12], in which the parent and daughter decays can be linked by means of a precise measurement of the deposition rate of each 99.6%-pure  $^{38}\text{Ca}$  sample. The major contributions

to our overall uncertainty came from the uncertainties in the known half-life of  $^{38}\text{K}^m$  and in our experimental determination of the relative intensity of the small  $^{35}\text{Ar}$  contaminant in our collected  $^{38}\text{Ca}$  sources.

We remarked in the Introduction that the  $f$ -value for the  $^{38}\text{Ca}$  superallowed transition is already known to  $\pm 0.03\%$  [2]. Now that we have measured the  $^{38}\text{Ca}$  half-life to  $\pm 0.08\%$ , only the branching ratio remains to be measured to comparable precision before this transition can take its place with the best-known superallowed transitions. With its relatively large calculated structure-dependent corrections, it will then contribute significantly to a comparative evaluation of the various sets of calculated correction terms [4], the ultimate goal being to reduce the uncertainties on these correction terms and consequently improve the precision of the CKM-matrix unitarity test. The branching-ratio measurement is currently in progress at our laboratory.

## ACKNOWLEDGMENTS

This work was supported by the U.S. Department of Energy under Grant No. DE-FG03-93ER40773 and by the Robert A. Welch Foundation under Grant no. A-1397.

- 
- [1] I.S. Towner and J.C. Hardy, *Rep. Prog. Phys.* **73**, 046301 (2010).
- [2] J.C. Hardy and I.S. Towner, *Phys. Rev. C* **79**, 055502 (2009).
- [3] I.S. Towner and J.C. Hardy, *Phys. Rev. C* **77**, 025501 (2008).
- [4] I.S. Towner and J.C. Hardy, *Phys. Rev. C*, **82**, 065501 (2010).
- [5] G. Bollen, D. Davies, M. Facina, J. Huikari, E. Kwan, P.A. Lofy, D.J. Morrissey, A. Prinke, R. Ringle, J. Savory, P. Schury, S. Schwarz, C. Sumithrarachchi, T. Sun and L. Weissman, *Phys. Rev. Lett.* **96**, 152501 (2006).
- [6] R. Ringle, T. Sun, G. Bollen, D. Davies, M. Facina, J. Huikari, E. Kwan, D.J. Morrissey, A. Prinke, J. Savory, P. Schury, S. Schwarz and C.S. Sumithrarachchi, *Phys. Rev. C* **75**, 055503 (2007).
- [7] S. George, S. Baruah, B. Blank, K. Blaum, M. Breitenfeldt, U. Hager, F. Herfurth, A. Herlert, A. Kellerbauer, H.-J. Kluge, M. Kretschmar, D. Lunney, R. Savreux, S. Schwarz, L. Schweikhard and C. Yazidjian, *Phys. Rev. Lett.* **98**, 162501 (2007).
- [8] B. Blank, A. Bey, I. Matea, J. Souin, L. Audirac, M.J.G. Borge, G. Canchel, P. Delahaye, F. Delalee, C.-E. Demonchy, R. Domínguez-Reyes, L.M. Fraile, J. Giovinazzo, Tran Trong Hui, J. Huikari, D. Lunney, F. Munoz, J.-L. Pedroza, C. Plaisir, L. Serani, S. Sturm, O. Tengblad and F. Wenander, *Eur. Phys. J. A* **44**, 363 (2010).
- [9] J.A. Cameron and B. Singh, *Nuclear Data Sheets* **109**, 1 (2008).
- [10] K.G. Leach, C.E. Svensson, G.C. Ball, J.R. Leslie, R.A.E. Austin, D. Bandyopadhyay, C. Barton, E. Bassiachvilli, S. Ettenauer, P. Finlay, P.E. Garrett, G.F. Grinyer, G. Hackman, D. Melconian, A.C. Morton, S. Mythili, O. Newman, C.J. Pearson, M.R. Pearson, A.A. Phillips, H. Savajols, M.A. Schumaker and J. Wong, *Phys. Rev. Lett.* **100**, 192504 (2008).
- [11] V.E. Iacob, J.C. Hardy, J.F. Brinkley, C.A. Gagliardi, V.E. Mayes, N. Nica, M. Sanchez-Vega, G. Tabacaru, L. Trache and R.E. Tribble, *Phys. Rev. C* **74**, 055502 (2006).
- [12] V.E. Iacob, J.C. Hardy, A. Banu, L. Chen, V.V. Golovko, J. Goodwin, V. Horvat, N. Nica, H.I. Park, L. Trache and R.E. Tribble, *Phys. Rev. C* **82**, 035502 (2010).
- [13] R.E. Tribble, R.H. Burch and C.A. Gagliardi, *Nucl. Instr. and Meth. in Phys. Res. A* **285**, 441 (1989).
- [14] V.T. Koslowsky, E. Hagberg, J.C. Hardy, G. Savard, H. Schmeing, K.S. Sharma and X. J. Sun, *Nucl. Instr. and Meth. in Phys. Res. A* **401**, 289 (1997).
- [15] I. Kawrakow, *Med. Phys.* **27**, 485 (2000); I. Kawrakow and D.W.O. Rogers, NRCC Report PIRS-701, NRC, Ottawa (2003); <http://www.irs.inms.nrc.ca/EGSnrc/EGSnrc.html>.
- [16] J.F. Ziegler, <http://www.srim.org/> (2008).
- [17] R.W. Kavanagh, A. Gallmann, E. Aslanides, F. Jundt and E. Jacobs, *Phys. Rev.* **175**, 1426 (1968).
- [18] A. Gallmann, E. Aslanides, F. Jundt and E. Jacobs, *Phys. Rev.* **186**, 1160 (1969).
- [19] J. Zioni, A.A. Jaffe, E. Friedman, N. Haik, R. Schectman and D. Nir, *Nucl. Phys. A* **181**, 465 (1972).
- [20] H.S. Wilson, R.W. Kavanagh and F.M. Mann, *Phys. Rev. C* **22**, 1696 (1980).